Hydrogen permeation behavior and hydrogen-induced defects in 316L stainless steels manufactured by additive manufacturing

Jiwei Lin [a], Feida Chen [a], Feng Liu [b], Dexin Xu [a], Jing Gao [a], Xiaobin Tang [a,c,*]

[a] Department of Nuclear Science & Technology, Nanjing University of Aeronautics and Astronautics, Nanjing, 211106, China
[b] School of Science, Nanjing University of Science and Technology, Nanjing, 210094, China
[c] Key Laboratory of Nuclear Technology Application and Radiation Protection in Astronautics (Nanjing University of Aeronautics and Astronautics), Ministry of Industry and Information Technology, Nanjing, 211106, China

HIGHLIGHTS

- H permeation behavior and H-induced defect evaluation of 3D printed 316L SSs.
- Sub-grain boundaries act as rapid transportation channels for the H atoms.
- SLM 316L SS generated H-induced defects with more volume fractions than CR 316L SS.
- H softening effect occurred in both SLM and CR 316L SSs.

GRAPHICAL ABSTRACT
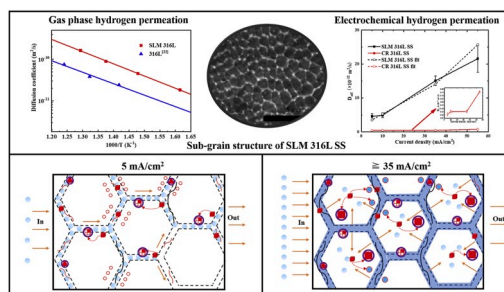
ARTICLE INFO

ABSTRACT

Additive manufacturing technology is a novel path to fabricate complex nuclear components. Considering the hydrogen (H) environment in which nuclear materials work, we proposed that the hydrogen resistance of structure materials should be considered as a deciding factor in the materials selection for nuclear application. In this work, we introduced H atoms into the selective laser melting (SLM) 316L stainless steel (SS) via two different H permeation methods and characterized its H permeation behavior and microstructure change. Results showed that the H diffusion rate in the SLM 316L SS was much higher than that in the cold-rolled (CR) one. The abundant sub-grain boundaries of the SLM 316L SS act as rapid transportation channels for the H atoms. H-induced defects which do not appear in the H charged CR 316L SS were observed in the H charged SLM 316L SS. H softening effect occurs in both SLM and CR 316L SS.

1. Introduction

Additive manufacturing (AM) technology, which is commonly known as 3D printing, can be utilized to complete tasks of material preparation and part forming simultaneously. It can significantly reduce the economic costs and production cycles of nuclear equipment due to its rapid prototyping. Considering its unique processing characteristics, AM technology is expected to solve the problem of complex nuclear equipment manufacturing [1]. However, structural materials in reactors have long-term served in hydrogen (H) environments. On the one hand,

---

H is generated in nuclear materials during neutron irradiation via transmutation. On the other hand, partial nuclear material is exposed to primary water containing dissolved H, thereby resulting in the abundance of absorbed H atoms. Massive H atoms and H-induced defects accumulating inside the material can lead to failures such as embrittlement, swelling, and accelerated corrosion. In exploring the application of AM technology in the field of nuclear materials, carrying out research on H resistance of typical nuclear structural materials formed by AM is necessary.

The 316L austenitic stainless steel (SS), due to its sufficient tolerance for corrosion and radioactivity, has been widely used for structural material in reactors [1]. Several years since the development of 316L austenitic SS, the processing technology in its preparation by selective laser melting (SLM) technology has become increasingly mature. Numerous studies indicated that SLM 316L SS has a typical microstructure different from that of traditional 316L SS. In 2015, Saeidi et al. observed that 316L austenitic SS formed by SLM technology by scanning electron microscopy (SEM) [2]. A nano-cellular sub-grain structure of extremely high density was observed inside the material grains. The sub-grain structure can be essentially stabilized even after annealing at 700 °C. In the following year, Trelewicz et al. [3] obtained a series of 316L SS with the average sub-grain size ranging from 200 nm to 1 μm by regulating the process parameters, such as laser scanning rate. In 2018, Qiu et al. [4] used a pulsed laser mode with different laser powers and scanning patterns to fabricate 316L SS samples by SLM. These research group confirmed that the laser-processed samples show both superior strength and ductility compared with conventionally manufactured counterparts due to the special microstructure containing cellular sub-grains and nano-inclusions. Variations in microstructures between the SLM 316L SS and the steel fabricated by traditional process does not only cause the changes in mechanical properties and corrosion resistance [1–6] but also have a trapping effect on He atoms [7], thereby effectively affect the formation of He bubbles. However, the effects of the structure on H atoms and H-induced defects remain unclear. Considering that H atoms and H-induced defects have a detrimental effect on the structure and properties of the material, evaluating the SLM-fabricated 316L SS under the H environment is extremely necessary.

In the present work, the H permeation behavior of the SLM 316L SS at different temperatures was investigated via gas-phase H permeation. Electrochemical H permeation was also used to introduce H atoms into the SLM 316L SS samples to explore the diffusion behavior of H atoms inside the material with different surface H concentrations. Combined with positron lifetime spectrum technique and the electrochemical H permeation results, we analyzed the defect information and the H diffusion mode of SLM 316L SS. We also conducted Vickers hardness tests to investigate the macroscopic mechanical properties before and after H charging. For comparison, the same experiments were further carried out on traditional cold-rolled (CR) 316L SS. The result showed that the SLM 316L SS had a unique H permeation characteristic different from that of CR 316L SS. According to the analysis of microstructure evolution of the two materials, the fundamental mechanisms for the special H permeation behavior in SLM 316L SS were revealed.

2. Experimental

2.1. Material preparation

Two 316L austenitic SSs were used for this study. The SLM 316L SS sample used in the experiment was provided by Xi'an Bright Laser Technologies Co., China, and the fabrication parameters were the same as that of a previous study [7], as shown in Table 1. The CR 316L SS was purchased from Wuxi Xinguangda Stainless Steel Co., Ltd. The chemical compositions of the two materials are listed in Table 2.

The SLM 316L SS samples were divided into two groups. The first group was disk samples with dimensions of 20.0 mm × 0.2 mm were

Table 1
Process parameters of SLM 316L austenitic stainless steel.

Power (W)	Scanning rate (mm/s)	Line spacing (mm)	Atmosphere	Spot diameter (μm)
200	850	0.1	Ar	70

Table 2
Nominal chemical compositions (wt%) of two kinds of 316L SS.

	Cr	Ni	Mo	Mn	Si	C	S	P
SLM	17.17	10.45	2.22	1.20	0.52	0.017	0.014	0.031
CR	16.64	10.05	2.02	1.18	0.44	0.020	0.002	0.031

used for Gas-phase H permeation experiment. Another group of SLM and CR 316L SS samples were used for electrochemical H permeation experiments. Both two 316L austenitic SSs were processed into the rectangular pieces of 20.0 mm × 30.0 mm × 0.5 mm by wire cutting, grounded with SiC papers, and polished to the mirror surface. The sample was plated with Ni on one side, and the compositions of the Ni-plated solution are presented in previous studies [8,9]. The purpose is to suppress the surface effect (H + H = H_2) occurring on the anode and protect the metal from corrosion, so as to guarantee that only hydrogen oxidation current is detected. According to relevant studies [10] the following optimum Ni plating process parameters were selected: the current density of Ni plating of 10 mA/cm^2 and the plating time of 5 min.

2.2. Gas-phase H permeation

Hydrogen gas-driven permeation (GDP) experiment with the pressure of 1.013×10^5 Pa was performed on a GDP system in the Institute of Plasma Physics, Chinese Academy of Sciences. The detailed description of the GDP device and the experimental procedure was shown in Liu [11]'s work. The temperature range of the GDP experiment was selected to be 623 K–773 K which is in line with commercial reactors operating temperature range [12].

2.3. Electrochemical permeation

The double electrolytic cell electrochemical permeation method proposed by Devanathan-Stachurski [13] was used to infiltrate H atoms into the specimens in the present work. The specimen was sandwiched between two electrolytic cells with an exposed area (effective area of H charging) of 1.77 cm^2 to solution as working electrodes. One side of the specimen is a H charged cell, which is also called a cathode cell, containing 0.2 mol/L NaOH and 1% Na_2S. In this cell, the specimen acted as cathodic where H^+ obtains e^- becoming H and penetrated the specimen. The cathodic cell was connected to a programmable DC-regulated power supply HSPY-36-03 ensuring that the charging current was constant. The Ni-plated side of the specimen faced the additional cell called anodic cell, containing 0.2 mol/L NaOH. The specimen acted as anodic where infiltrated H can be electrolyzed into H^+, thereby increasing the anode current. The anodic cell was connected to a CHI600E electrochemical workstation, which applied a constant potential to ensure the ionization of H atoms. A Hg-HgO electrode was used as a reference electrode for the anodic side and two platinum electrodes were used as auxiliary electrodes. After connecting the instruments shown in Fig. 1, we added electrolyte to the anode cell and the anodic side was set to an oxidation potential of 0.15 V (vs. Hg/HgO). When the current density decreased to <0.1 μA cm^{-2}, we started charging the H in the cathode cell. Both cells were maintained at a constant temperature of 298 ± 1 K by a water bath throughout the experiment.
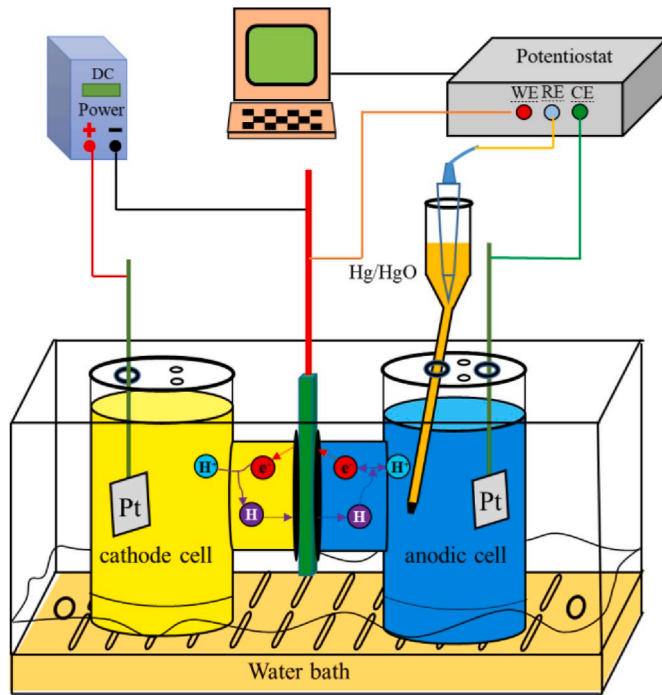
Fig. 1. Scheme of experimental device for H permeation experiment.

2.4. Data analysis method of H permeation

The temperature dependence on the measured H permeability (mol/m/s/Pa$^{1/2}$) in metals can be presented by the following [14]:

$$\varphi = \frac{J_\infty \, L}{P_1^{\frac{1}{2}}} \qquad (1)$$

where J is the steady-state diffusion flux (mol/m^2/s), P_1 is the equilibrium H pressure (Pa) at the inlet surfaces, and L is the sample thickness (m).

Permeability Φ (mol/m/s/Pa$^{1/2}$) and diffusion coefficient D (m^2/s) with temperature changed following the Arrhenius relationship [14], as follows:

$$\varphi = \varphi_0 \exp\left(-\frac{E_\varphi}{RT}\right) \qquad (2)$$

$$D = D_0 \exp\left(-\frac{E_D}{RT}\right) \qquad (3)$$

where Φ_0 and D_0 are the pre-exponential coefficients; E_Φ (KJ/mol) and E_D (KJ/mol) are the penetration and diffusion activation energies, respectively; R is the gas constant, and T is the temperature during the charging process.

The hydrogen permeation flux J_∞, the effective diffusion coefficient and the apparent H concentration were determined as follows [15]:

$$J_\infty = \frac{I_\infty}{FA} \qquad (4)$$

$$D_{eff} = \frac{L^2}{6t_{0.63}} \qquad (5)$$

$$C_{app} = I_\infty \, L/DFA \qquad (6)$$

D_{eff} is the effective diffusion coefficient (m^2/s), C_{app} is the apparent H concentration (mol/m^3), I_∞ is the anode steady-state current (μA) and A is the effective area of H charging (m^2). $t_{0.63}$ is the time when 63% of the steady-state current density was reached. F is the Faraday constant.

2.5. Characterization

Optical microscopy (OM, Zeiss Scope A1), SEM (Apollo 300) and TEM (Tecnai G2 F20 S-Twin) were used to observe the SS microstructure. TEM specimens were prepared by a standard double-jet procedure (7 vol% per-chloric acid and 93 vol% ethanol with a voltage of 65 V at -25 °C). To explore the evolution of defects before and after H charging, we performed the positron annihilation lifetime spectrum (PALS) using a fast-slow coincidence system. The positron source ^{22}Na was deposited on a titanium foil and sandwiched between two pieces of the samples. The lifetime resolution was 210 ps and each of the lifetime spectra collected 1.5×10^6 counts. Two standard single crystal Ni samples of an area of 1 cm^2 were used to modify source contributions (228 ps, 14.15%). The obtained PALS data were fitted with three lifetimes by using LT9.0 program. Fit variance in the data analysis process was between 0.9 and 1.1. The third life component τ_3 was between 1 ns and 2 ns, and its relative intensity I_3 was <0.5%. This finding can be considered as the influence of source component and surface annihilation, which was disregarded in the experimental analysis. Vickers hardness test (MHVD-30AP) was performed to investigate the change in sample hardness before and after H charging. The load was 9.8 N with the holding time of 20 s.

3. Results and discussion

3.1. Pre-charged specimen microstructure

Figs. 2(b) and (e) show the CR and SLM 316L SS microstructures under an OM at the same magnification, respectively. The martensitic phase can be observed as black precipitates in the CR 316L SS. XRD spectra in Fig. 2(a) also confirmed the existence of the martensitic phase. In a comparison to that, SLM 316L SS shows a unique layer band structure without any precipitates, and it has a single-phase austenite structure. Further, from the SEM micrographs of CR 316L SS with higher magnification in Fig. 2(c), we measured that the average grain size is approximately 11.28 μm. In contrast to that, SLM 316L SS in Fig. 2(f) presents a special cellular sub-grain structure with a grain diameter of approximately 480 nm. The grain of SLM 316L SS is obviously much finer than that of CR 316L SS. The roles of the grain boundaries and precipitate phases played in the hydrogen diffusion behaviors have been discussed in the previous studies[16–21]. It is reported that the precipitation phase, e.g., the Sigma phase and M$_{23}$C$_6$ are usually found near the grain boundary in SLM [16] and CR 316L SS [17]. However, all of them were proved to be ineffective hydrogen traps in austenitic steels [18,19]. In the other hand, Mine et al. [19] compared the influence of sigma phase in 310S austenitic SS to the hydrogen diffusion and that of grain boundaries. He indicated that short-circuit diffusion is enhanced through an increased fraction of the grain boundaries. With further research, grain boundary has been widely accepted as a main factor affecting hydrogen diffusion in austenite SS, but the detailed interaction mechanism between hydrogen and grain boundaries is unclear to date. Alefeld et al. [20]suggested that the grain boundaries are traps for H atoms, which can capture H atoms, thereby hindering H diffusion. However, Jost et al. [21] stated that the atoms at the grain boundaries are irregularly arranged, the structure is loose, and H atoms easily pass through loose regions. Since the SLM 316L SS possesses much higher grain boundary volume than the CR 316L SS, the hydrogen permeation behaviors in the SLM 316L SS and the CR 316L SS were compared in this work.

3.2. H permeation transient profiles

3.2.1. Gas phase H permeation

The evolution of the downstream H permeation flux through SLM 316L SS is shown in Fig. 3(a). As the temperature of the H permeation experiment increased, the H breakthrough time decreased and the
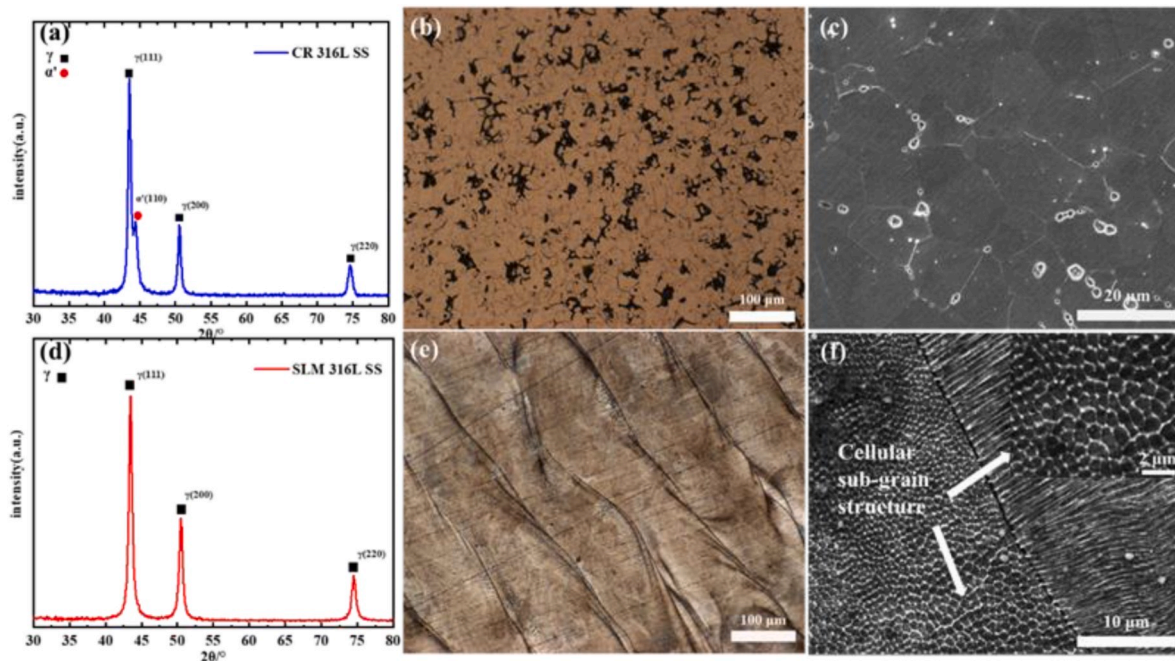
Fig. 2. Microstructure of CR and SLM 316 SSs; (a) XRD pattern (b) OM micrograph and (c) SEM micrograph of CR 316L SS, (d) XRD pattern (e) OM micrograph and (f) SEM micrograph of SLM 316L SS.
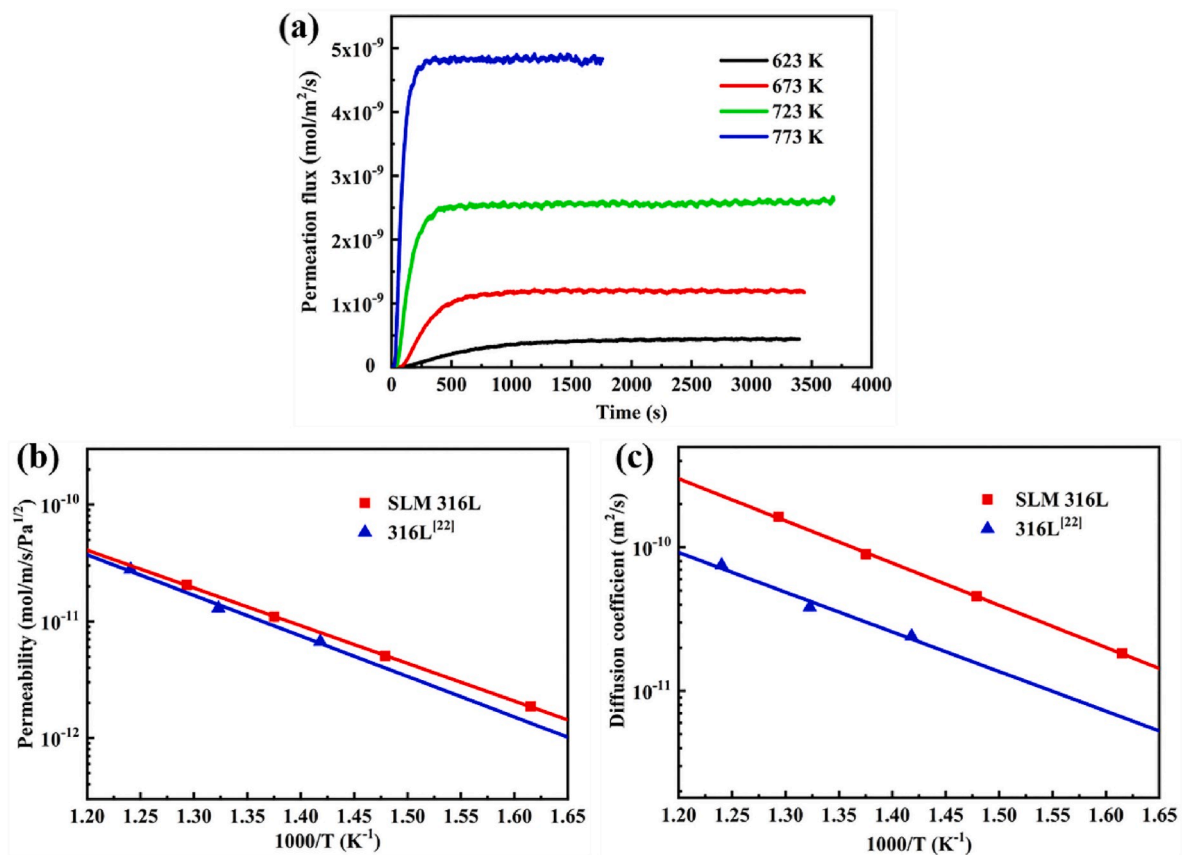

Fig. 3. (a) H permeation flux vs. SLM 316L SS time with the upstream driven pressure of 1.013×10^5 Pa; Temperature dependence of permeability (b) and diffusion coefficient (c) of H in SLM 316L SS compared with traditional 316L SS [22].

permeate flux increased, because the H atom activity, thermal motion and diffusion rate in the steel increase with the increase in temperature. Fig. 3(b) shows the temperature dependence of the permeability

through the samples between SLM 316L SS and data from Xu [22]'s work. In Xu's work, the 316L samples bought from Goodfellow Co. were fabricated through traditional methods such as casting or CR, but were

not described in detail. The results showed that the H permeability of SLM 316 SS is slightly higher than that of 316L SS [22] at the temperature ranging from 623 K to 773 K. The temperature dependence of the measured H permeability (mol/m/s/Pa$^{1/2}$) in SLM 316L SS can be presented by the following equation:

$$\varphi_{\text{SLM316L}} = 3.08 \times 10^{-7} exp(-61.804(KJ/mol)/RT) \tag{7}$$

Meanwhile, the temperature dependence on the obtained of H permeability in 316L [22] SS obtained by the same device [11] was presented by the following equation:

$$\Phi_{316L[22]} = 4.12 \times 10^{-7} exp(-64.713(KJ/mol)/RT) \tag{8}$$

It is widely proved that H permeability cannot be influenced by defects in austenitic SS [14]. During the process of GDP experiments, oxide films could form and influence the results [22]. The E_{Φ} is essentially unaffected by the oxidation [22] and defects but by the element composition and lattice structure [14]. Since the influence factors of the two 316L steels are similar, there is little difference in E_{Φ}. The pre-exponential factor Φ_0 represents the sensitivity of permeability to temperature. Studies [23,24] have shown that material fabricated by SLM has a higher oxidation resistance than that manufactured by traditional craft. Sub-grain boundaries can act as diffusion channels for O and Cr, thereby forming network of oxides along these boundaries. This in turn slows down the overall volume diffusion of O and Cr into the matrix, and improves oxidation resistance. Therefore, the oxidation degree of SLM 316L would be less than that of traditional 316L under similar experimental conditions, resulting in a slightly higher permeability. The value of the pre-exponential factor Φ_0 indirectly reflects the

sensitivity of the oxidizability to temperature.

Fig. 3(c) shows the H diffusion coefficients of SLM and traditional 316L SSs [22]. The diffusion coefficient of SLM 316L SS was approximately fourfold larger than traditional 316L SS [22] at the temperature ranging from 623 K to 773 K. The H diffusion coefficient (m^2/s) in SLM 316L SS can be expressed by the following:

$$D_{SLM316L} = 1.01 \times 10^{-6} \exp(-56.156(KJ/mol)/RT) \tag{9}$$

The H diffusion coefficient in 316L [22] SS was given by the following [22]:

$$D_{316L[22]} = 1.38 \times 10^{-7} \exp(-50.91(KJ/mol)/RT) \tag{10}$$

E_D is the activation energy barrier associated with the predominant diffusion process. And it is mainly affected by hydrogen trapping sites in the material like dislocations and grain boundaries [25]. Since many sub-grain boundaries, which can act as hydrogen trapping sites, exist in SLM 316L SS, the E_D (56.156 kJ/mol) of SLM 316L SS is greater than that of 316L fabricated by traditional craft (50.91 kJ/mol) The pre-exponential factor D_0 is changes with the microstructure and so depends on the mean free path of hydrogen into materials [25]. Thus it is relative to the probability of hydrogen atoms jumping [26] and diffusion rate of hydrogen [27] in the material. The results show that the D_0 of SLM 316L SS is an order of magnitude larger than that of 316L manufactured by traditional processes which indicate a higher hydrogen diffusion rate in SLM 316L SS. The sub-grain boundaries in SLM 316L SS may not only have trapping effect on H, but also accelerate H diffusion.

After comparison, we can conclude that the H diffusion rate of SLM 316L SS was faster than that of traditional 316L SS from 623 K to 773 K.
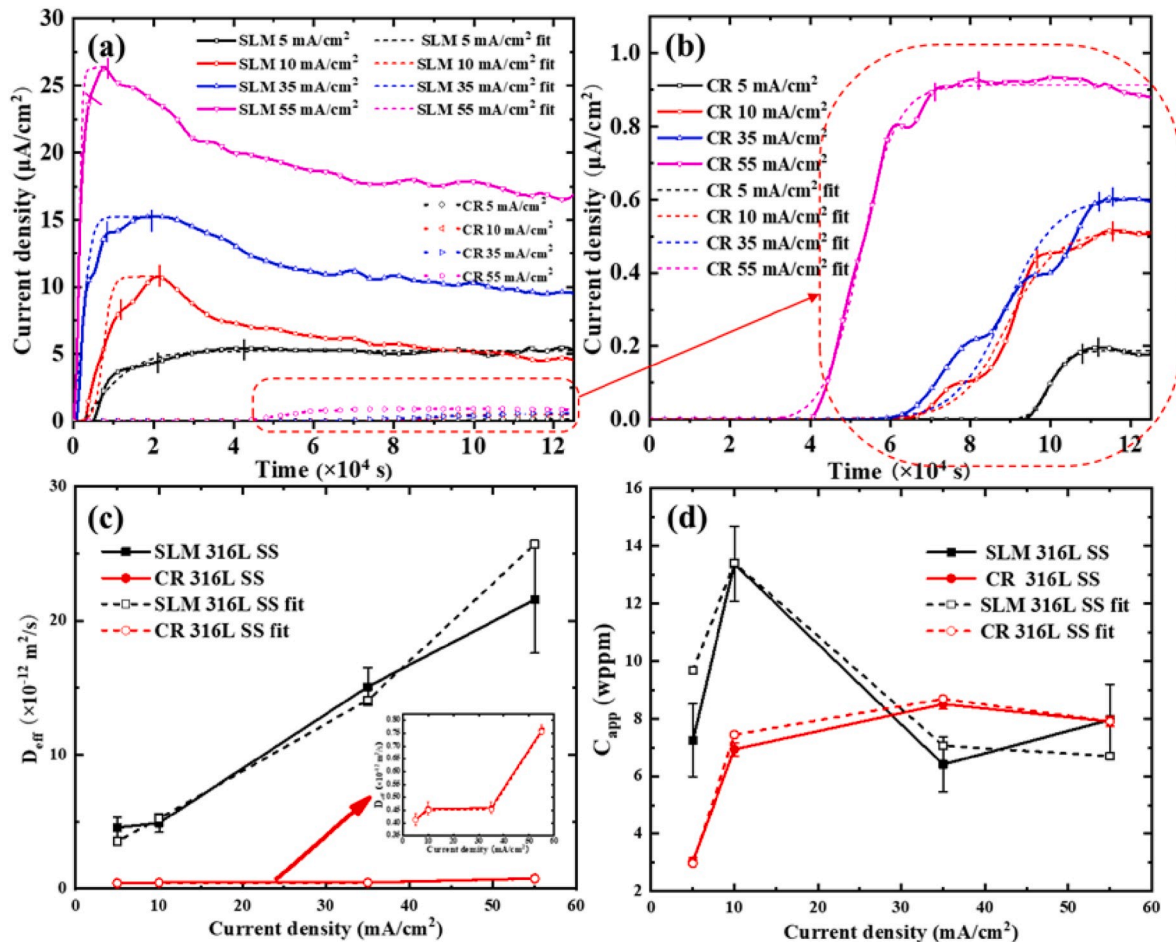

Fig. 4. H permeation transient profiles of two steels at different cathodic charging current densities: (a) SLM and CR 316L SS; (b) CR 316L SS; Comparison of (c) effective diffusion coefficient; (d) apparent H concentration as a function of cathodic current density for SLM and CR 316L SSs.

3.2.2. Electrochemical H permeation

Figs. 4(a) and (b) show the H permeation curves of SLM and CR 316L SSs under different H charging currents. In order to avoid the disturbance of the error, the steady-state current density values within a certain range were selected to calculate the kinetic parameters of H permeation. The range is from the nearest inflection point to the maximum value of current density. The calculated results of D_{eff}, C_{app} and J_∞ are shown in Fig. 4 (c) and 4 (d) and Table 3. In addition, to obtain appropriate sigmoids, a prerequisite for using a simple analysis based on the $t_{0.63}$ parameter, we used Boltzmann function [28] to fit the curve, and calculated the relevant kinetic parameters. The results show that the experimental values are in good agreement with the fitting values. By comparing the results of different current density, the time of hydrogen penetration and reaching steady state decreases, and J_∞ and D_{eff} increase as the current density increasing. The promoting effect of charging current density on hydrogen diffusion is obvious [29,30]. Unlike other kinetic parameters, the C_{app} increased at the beginning and then decreased possibly because the number of H atoms generated per unit time increased with the increase in current. Hence, the probability of H atoms recombined into H molecules increases, thereby decreasing the number of H atoms beneath the cathodic surface [29].

The results between hydrogen diffusion coefficient in SLM 316L SS calculated from gas-phase and electrochemical permeation was compared in Fig. 5. The D_{eff} of SLM 316L SS was 4.57×10^{-12} m^2/s at the charging current density of 5 mA/cm^2. However, according to the results got from gas phase hydrogen permeation, the effective diffusion coefficients in SLM 316L SS is estimated to be 1.4478×10^{-16} m^2/s. Many researchers have found this deviation in their experiments [25] and simulations [31]. Such deviations were attributed to the stronger effect of grain boundary on hydrogen diffusion [32] at room temperature than that at higher temperature. Hydrogen sinks only affect hydrogen diffusion at a certain low temperature. However, the mechanisms of electrochemical hydrogen permeation and gas phase hydrogen permeation are different. Brass et al. [33] found that the hydrogen concentration measured after cathodic charging at 368 K exceeds the values measured after charging in the gas phase at much higher temperatures. The equivalent hydrogen pressures exerted on the sample's surface during cathodic charging are far greater than that usually be used in the autoclaves, resulting in a larger D_{eff} of H. Above all, this deviation may be due to the contribution of sub-grain boundaries, or the difference between the two permeation method.

The hydrogen kinetic parameters of SLM and CR 316L SS was compared. It was found that the H penetration time and time to reach steady-state were less, and the D_{eff} and J_∞ were larger in SLM 316LSS than that in CR. This result proved that H has a stronger diffusivity in SLM 316L SS than that in CR 316L SS. Based on the microstructure differences between the two 316L SS, we concluded that the sub-grain boundary plays a role in promoting hydrogen diffusion at RT.

Both gas phase H permeation and electrochemical H permeation experiments results show a stronger hydrogen diffusivity in SLM 316L SS

Table 3
Effective diffusivity D_{eff}, apparent H concentration C_{app} and hydrogen permeation flux J_∞ versus different H charged current densities during the permeation experiment.

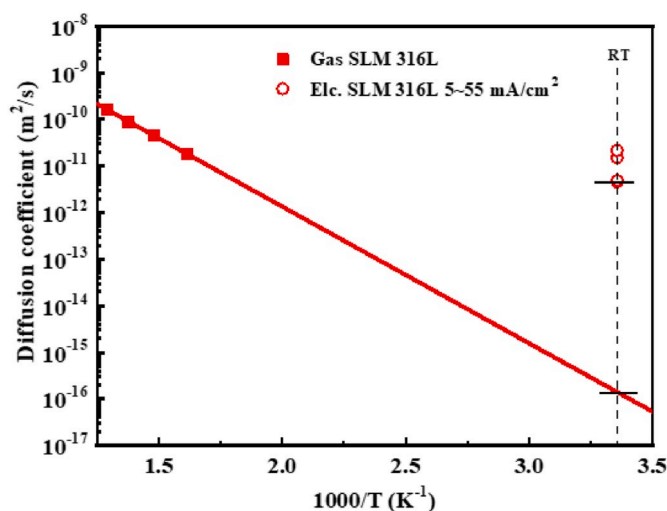| Current density (mA/cm^2)	D_{eff} ($\times 10^{-12}$ m^2/s)		C_{app} (wppm)		J_∞ ($\times 10^{-7}$ mol/m^2/s)	
	SLM	CR	SLM	CR	SLM	CR
5	4.57 ± 0.78	0.41 ± 0.002	7.24 ± 1.27	3.05 ± 0.13	5.12 ± 0.76	0.20 ± 0.01
10	4.90 ± 0.70	0.46 ± 0.003	13.38 ± 1.30	6.94 ± 0.23	10.34 ± 1.15	0.50 ± 0.05
35	15.1 ± 1.4	0.46 ± 0.002	6.41 ± 0.95	8.51 ± 0.18	15.19 ± 0.84	0.62 ± 0.01
55	21.6 ± 4.0	0.76 ± 0.002	7.96 ± 1.24	7.90 ± 0.16	26.31 ± 1.37	0.95 ± 0.02

Fig. 5. Comparison of effective diffusion coefficient of SLM 316L SS between the electrochemical and the gas phase experiments.

than 316L SS fabricate by traditional handicraft. To explore the effect of high H permeability on SLM 316L SS, we characterized the changes in the microstructure after the sample H permeation.

3.3. Changes in microstructure

3.3.1. PALS

PALS is a widely used method in characterizing atomic-scale defects in materials. Hydrogen damage or hydrogen embrittlement (HE) of iron and stainless steels has been investigated by many authors using PALS [34–36]. Chen et al. [35] suggested that H can cause structural defects and H damage in stainless steels. The lifetime of vacancies and dislocations was approximately 140–200 ps. The lifetime of vacancy clusters formed by multiple vacancies was approximately 200–400 ps, and the lifetime of H damages such as H bubbling and cavities was approximately 400–500 ps [35]. These values will serve as references for analyzing our experimental results. Fig. 6 and Table 4 show the lifetime components τ_1 and τ_2 and relative intensities I_1 and I_2 as a function of current density in SLM (panel a) and CR 316L SSs (panel b). The short lifetime component τ_1 represented the weighted average of the lifetime of the positron annihilating in the free volume of the sample and the lifetime of the small structural defect. Meanwhile the long lifetime τ_2 component represented the lifetime value of the annihilation of positrons in large defects. The lifetime values changed significantly within the range of the current density of hydrogenation in this study, indicating that the microstructure of the material evolved.

Fig. 6(a) shows that τ_1 of SLM 316L SS was 120ps before H charging; this value was slightly larger than the lifetime ($\sim$106 ps) of positron annihilation in the SS free state [34]. Sun et al. [7]indicated that SLM 316L SS has several sub-grain boundaries and dislocations, and positrons tend to annihilate in these defects, thereby resulting in an increase in τ_1 [37]. τ_1 increased with the increase in current density, which implied that small-size defects, such as vacancies and dislocations induced by H appeared, and the size of defects increased [35] The τ_2 of SLM 316L SS before H charging was 325 ps (between 200 and 400 ps), thereby indicated that the sample itself has large vacancy clusters of 5–10 vacancies [38]. However, the number of clusters was small (the intensity I_2 was only 1.76%). A slight increase in τ_2 (325–339 ps) and I_2 (1.7%–2.8%) at current density of 5 mA/cm^2 manifested that the size and the number of vacancy clusters increased slightly. Sugimoto et al. [39] illustrated that H atoms can reduce the vacancy formation energy and binding energy and become the cores of vacancy nucleation and aggregation in Fe. Therefore, H can increase the size and number of vacant clusters. The τ_2 suddenly decreased to 250 ps at the current
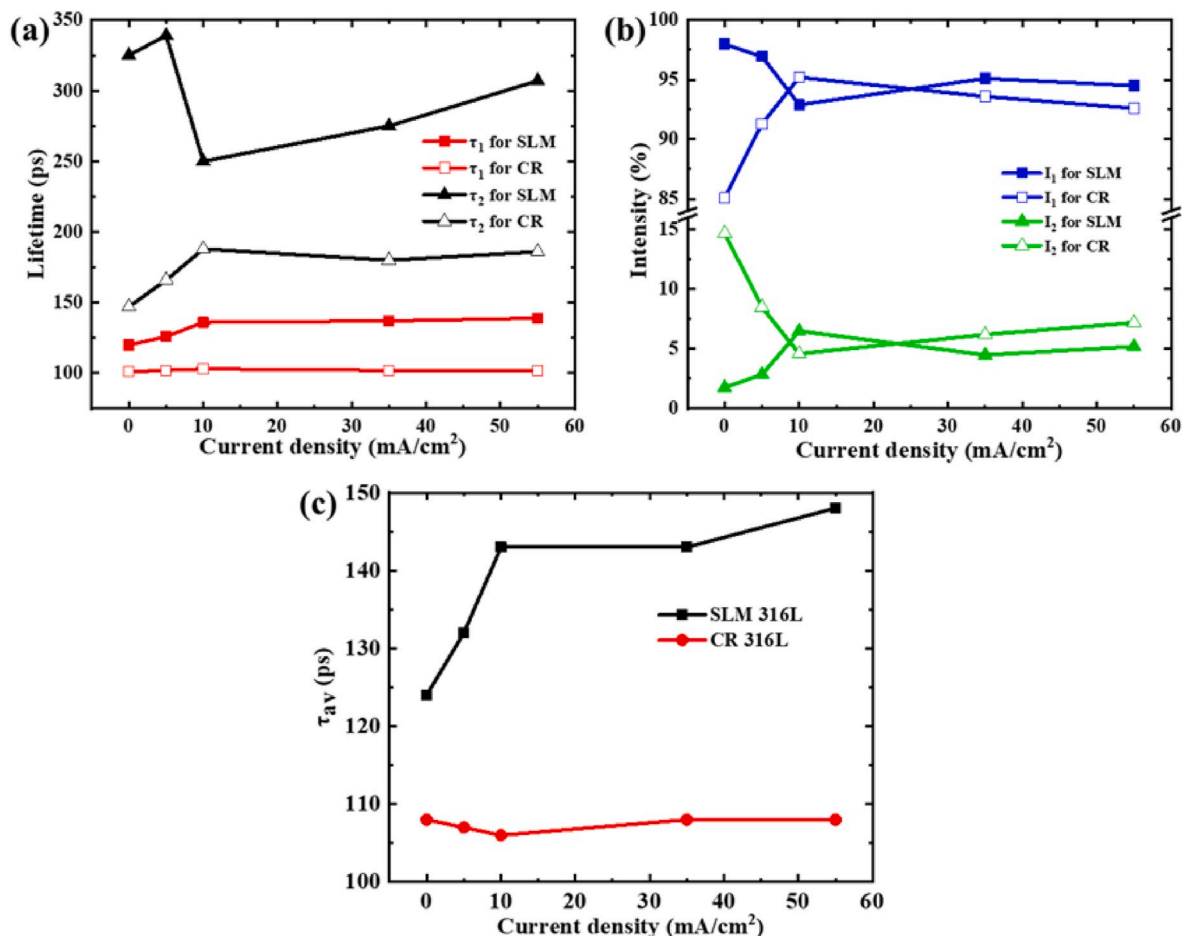
Fig. 6. Variations in positron lifetime parameters of (a) τ_1 and τ_2 and intensity parameters (b) I_1 and I_2 versus current density of SLM and CR 316L SS; (c) Comparison of average positron lifetime as a function of cathodic current density for SLM and CR 316L SSs.

Table 4
Positron annihilation lifetimes and their intensities for H-charged SLM and CR 316L SSs.

Material	Current density (mA/cm^2)	τ_1	τ_2	I_1	I_2	τ_{av}
SLM 316L SS	0	120	325	97.9	1.7	124
	5	126	339	96.9	2.8	132
	10	136	250	92.9	6.5	143
	35	137	275	95.1	4.5	143
	55	139	307	94.5	5.2	148
CR 316L SS	0	101	147	85.1	14.7	108
	5	102	166	91.3	8.4	107
	10	102	188	95.2	4.6	106
	35	103	180	93.6	6.2	108
	55	102	186	92.6	7.2	108

density of 10 mA/cm^2. He et al. [36] reported that if the vacancies contain H atoms, the positron lifetime can decrease due to the overlap of electrons of H atoms with trapped positrons. Hence, the H atoms combined with the intrinsic vacancy clusters in the SLM 316L SS form a complex, thereby decreasing τ_2. Meanwhile, I_2 increased from 2.8% to 6.5%, which suggested that the new vacancy clusters of 3–5 vacancies (232–304 ps) appeared [38]. τ_2 gradually increased with the increase in the current density of >10 mA/cm^2, which indicated the size of the defects increased with the increase in current density. We will analyze the effect of different hydrogen permeation current densities on the formation of hydrogen-induced defects in the next section.

Fig. 6(b) shows that as the H charging current increased to 10 mA/cm^2 in CR 316L SS, τ_1 does not change, τ_2 increased (from 147 ps to 188

ps (belongs to 140–200 ps)), but I_2 decreased (from 14.4% to 4.6%). This result was observed because small structure defects, such as dislocations induced by cold working, converged into large size defects. I_2 gradually increased (4.6%–7.2%) with the increase in current density from 10 mA/cm^2 to 55 mA/cm^2, and new defects may appear. To evaluate the overall information of the defects of the material after electrochemical H permeation, we used the average lifetime τ_{av} to judge [36], which was calculated using the following equation:

$$\tau_{av} = \frac{\tau_1 I_1}{I_1 + I_2} + \frac{\tau_2 I_2}{I_1 + I_2} \tag{11}$$

The results in Fig. 6(c) showed that with the increase in H charging current density, the average life of CR 316L SS is almost unchanged, thereby indicating that almost no new defect was formed during the H permeation process. By contrast, the average life of SLM 316L SS increased with the increase in H charging current, thereby indicated that the total volume fraction of defects gradually increased. According to the results of H-induced defects, the CR 316L SS had higher H resistance than SLM 316L SS at room temperature.

3.3.2. Hydrogen Permeation Mechanism in SLM 316L SS

In the case of hydrogen permeation, different hydrogen charging current densities lead to different changes in the microstructure, possibly due to distinctions between hydrogen diffusion rates caused by different current densities. It is widely believed that H atoms would be captured by hydrogen sinks when they enter into the material. When the hydrogen atom sink is saturated, the subsequent incoming hydrogen atoms can diffuse into the crystal [40]. Furthermore, hydrogen naturally

escapes from some reversible traps with a velocity. If the hydrogen diffusion rate is not fast enough, hydrogen traps will not be filled up. Yazdipour [32] revealed that hydrogen atoms start diffusing through the boundaries in the early stages of diffusion because the diffusion rate in the boundaries is several orders of magnitude higher than the interior of the grains. The results of gas phase and electrochemical hydrogen permeation had proved that the sub-grain boundary has the effects of trapping and promoting diffusion of hydrogen atoms. Therefore, as shown in Fig. 7, if the hydrogen diffusion rate is slow (5 mA/cm^2), most of the hydrogen will always diffuse along the sub-grain boundary. However, if the hydrogen diffusion rate reaches a certain level ($\geq$10 mA/cm^2), the hydrogen in the grain boundary will saturate and spread to the interior of sub-grains, resulting in more defects in the interior.

As shown in the PALS results, τ_2 and I_2 increase slightly when the current density reach 5 mA/cm^2, According to the assumption in the previous paragraph (most of hydrogen atoms diffuse along the sub-grain boundary), the intrinsic vacancy clusters (V-cluster) inside the sub-grain boundaries was combined with the hydrogen-induced vacancy, resulting in larger sizes. H-induced V-clusters would also form inside the sub-grain boundaries, resulting in an increase in defect density and an increase in I$_2$, as shown in Fig. 7(b). Oudriss [25] researched grain-boundary effects on diffusion and trapping of hydrogen in pure nickel. He proved that hydrogen promotes formation of vacancies in GBs while its diffusion along GBs. This supports the view that H-induced vacancy clusters can form inside the sub-grain boundaries.

Fig. 7(c) showed that H had a tendency to diffuse into the sub-grain with the current density of 10 mA/cm^2. Yazdipour [32] used the Cellular Automaton technique combined with the finite difference method to simulate the diffusion of hydrogen in X70 steel. It was found that there was a concentration gradient at the grain boundary towards the inside of the grain. The closer to the grain boundary, the higher hydrogen concentration was. The PALS result showed that τ_2, decreased to 250 ps with a current density of 10 mA/cm^2, and the hydrogen atom has a tendency to diffuse into the sub-grain at this time. The intrinsic vacancies near the sub-grain boundary will form into H-V complex with hydrogen. The number of equilibrium vacancies in metal crystals increases significantly at high temperatures. If the cooling rate is low, excess vacancies will annihilate on the free surface, grain boundaries, sub-grain boundaries and dislocations due to thermal movement during cooling. If the

material is quenched from high temperature, the vacancies will not disappear and be "frozen". Most of the vacancies remain at low temperature, which greatly increases the number of vacancies around the sub-grain boundary. Cooling rates for materials fabricated by SLM is about 10^6 K/s [41]. Thus, such structure (vacancies surround sub-grain boundaries) can be formed in SLM alloys [42]. As shown in Fig. 7 (c), hydrogen forms into a complex with the vacancies around the sub-grain boundary. In the meantime, some hydrogen-induced vacancy clusters also appear around the sub-grain boundary, resulting an increase in I_2. When the hydrogen charging current density become larger, more and more hydrogen atoms will diffuse to the center of the sub-grain, as shown in Fig. 7(d). Meanwhile, more vacancies generated inside the sub-grains. With the action of hydrogen atoms, these vacancies merge with the original formed small-sized vacancy clusters, leading τ_2 to increase. The schematic shown in Fig. 7 is an exaggeration of the main diffusion pattern, in which a small amount of hydrogen would diffuse into the sub-grains even at a small diffusion rate.

The theory of plasticity localization in the metal with the effect of hydrogen became widespread. Hydrogen promotes the migration and merger of dislocations [43]. As shown in the TEM results in Fig. 7 (a), dislocations are attached to the sub-grain boundaries of SLM 316L SS. It is found that many dislocations were produced in CR 316L SS due to cold rolling [44]. Therefore, these dislocations can also merge with the effect of hydrogen. As the current density increases, the hydrogen diffusion rate increases, and the local stress field around the hydrogen also changes, causing the change of dislocation structure. Therefore, the PALS results (τ_1 of SLM and τ_2 of CR) changed.

Changes in the microstructure of the material often result in changes in the macroscopic mechanical properties of the material. C. Senöz et al. [45] mentioned that hydrogen embrittlement could even occur at concentrations as low as 0.1 ppm. Hence, apparent H concentration (3.05–13.38 ppm) measured by us is enough to transform the mechanical properties. We measured the changes in the hardness of the two 316L SSs before and after H permeation to characterize the effect of the interaction of H and defects in the material.

3.4. Change in hardness

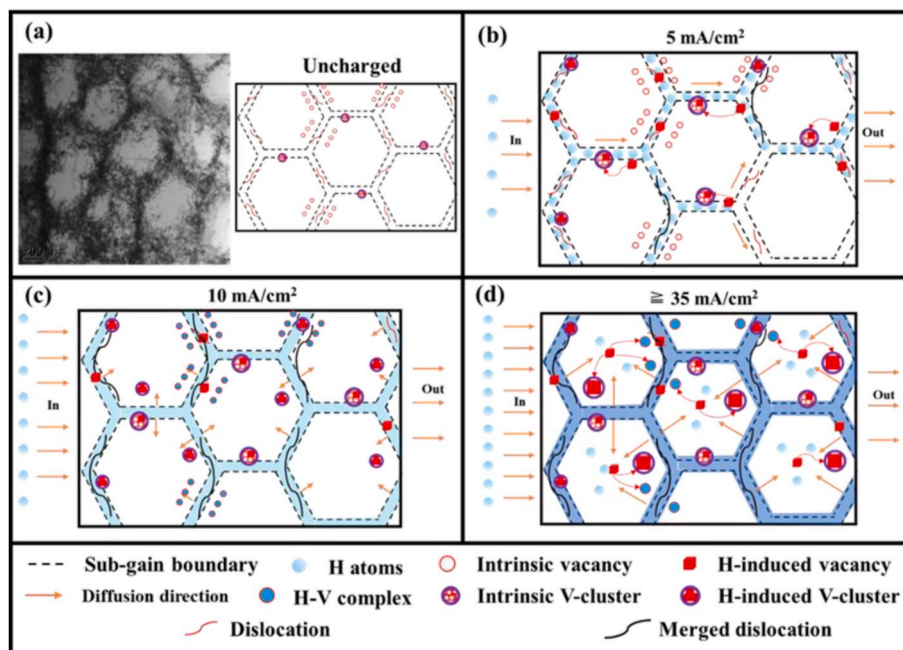Fig. 8 displays the change in Vickers hardness of SLM and CR 316L

Fig. 7. Hydrogen permeation mechanism in SLM 316L SS.
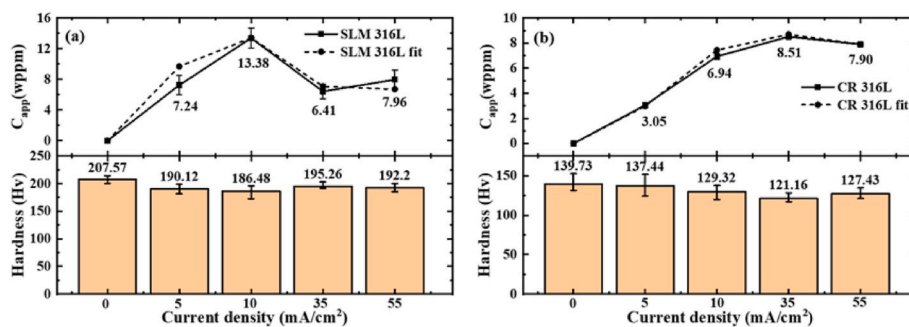
Fig. 8. Vickers hardness of 316L SS after H permeation at different H permeation current densities: (a) SLM 316L SS; (b) CR 316L SS.

SSs after H permeation. SLM 316L SSs exhibited higher hardness than CR 316L SS. It can be explained that the SLM 316L SSs possess higher grain boundary volume fractions than the CR ones. The grain boundaries will prevent the movement of dislocations and will cause the increase in hardness of the SLM 316L SSs. After H permeation, the hardness of both 316L SSs decreased. The type of defects which can interact with hydrogen to cause changes in hardness needs to be addressed. Under normal circumstances, point defects have minimal effect on the mechanical properties of metals; they only harden the material by interacting with dislocations and hindering the movement of dislocations [46]. Depending on a molecular dynamic simulation, single vacancies decorated with H atoms cannot obstruct the dislocation motion in α-Fe [47]. Considering that the hydrogen-induced defects appeared in SLM 316L SS but not in CR one, H softening effect occurred in both SLM and CR 316L SSs, we judged that the interaction between the original defects in the material and hydrogen is the main factor to cause the change in hardness after hydrogen charging. Since previous studies [7,14] and PALS results (τ_1 of SLM 316L SS > 106ps and τ_2 of CR 316L SS > 140 ps) indicated that dislocations were found in both SLM and CR 316L SSs. Therefore, the interaction between H and dislocation may be the main factor to cause the change in hardness in stainless steel. On the one hand, the H atoms can be segregated at the core of the dislocations to weaken the binding force of the core atoms. On the other hand, the elastic strain energy of the dislocations can be reduced by H [48,49]. Thus, the mobility of dislocations can be promoted by H atoms. This mechanism can also explain the evaluation of dislocation in PALS results. Given that H can enhance the movement of dislocations, the material appeared macroscopically softened.

4. Conclusion

In summary, hydrogen permeation behaviors in 316L SS fabricated by SLM and CR were investigated by gas and electrochemical hydrogen permeation techniques. We also characterized their microstructure and mechanical property changes by PALS, XRD and Vickers hardness test. The results show that H diffused faster in SLM 316L SS with the contribution of sub-grain boundaries. Due to the unique H permeation characteristic, SLM 316L SS generated hydrogen-induced defects with a higher total volume fraction than the CR one under the same H charging current density. However, these hydrogen-induced defects would not affect the hardness of the two steels. The main cause of hardness change may be the interaction between hydrogen and the original dislocation in the material. It is worth noting that the presently work has specifically revealed the internal effects of microstructure on hydrogen diffusion of SLM 316L SS, which was performed at room temperature and 623 K–773 K. Further parameter developments for studying hydrogen permeation behavior in SLM 316L SS details like temperatures, pressure and isotopic species of hydrogen are needed. Effect of hydrogen on mechanical properties such as tensile strength needs to be clarified in future work on this topic.

Declaration of competing interest

The authors declare that they have no known competing financial interests or personal relationships that could have appeared to influence the work reported in this paper.

Appendix A. Supplementary data

Supplementary data to this article can be found online at https://doi.org/10.1016/j.matchemphys.2020.123038.

References

[1] Y. Zhong, L.-E. Rännar, S. Wikman, A. Koptyug, L. Liu, D. Cui, Z. Shen, Additive manufacturing of ITER first wall panel parts by two approaches: selective laser melting and electron beam melting, Fusion Eng. Des. 116 (2017) 24–33.
[2] K. Saeidi, X. Gao, Y. Zhong, Z.J. Shen, Hardened austenite steel with columnar sub-grain structure formed by laser melting, Mater. Sci. Eng., A 625 (2015) 221–229.
[3] J.R. Trelewicz, G.P. Halada, O.K. Donaldson, G. Manogharan, Microstructure and corrosion resistance of laser additively manufactured 316L stainless steel, JOM 68 (2016) 850–859.
[4] C. Qiu, M. Al Kindi, A.S. Aladawi, I. Al Hatmi, A comprehensive study on microstructure and tensile behaviour of a selectively laser melted stainless steel, Sci. Rep. 8 (2018) 7785.
[5] J. Materials Science and Engineering AIsselin, R. Kasada, A. Kimura, Work hardening, sensitization, and potential effects on the susceptibility to crack initiation of 316L stainless steel in BWR environment, J. Nucl. Sci. Technol. 48 (2011) 1462–1470.
[6] Q. Chao, V. Cruz, S. Thomas, N. Birbilis, P. Collins, A. Taylor, P.D. Hodgson, D. Fabijanic, On the enhanced corrosion resistance of a selective laser melted austenitic stainless steel, Scripta Mater. 141 (2017) 94–98.
[7] X. Sun, F. Chen, H. Huang, J. Lin, X. Tang, Effects of interfaces on the helium bubble formation and radiation hardening of an austenitic stainless steel achieved by additive manufacturing, Appl. Surf. Sci. 467 (2019) 1134–1139.
[8] H. Huang, X. Tang, F. Chen, J. Liu, X. Sun, L. Ji, Radiation tolerance of nickel–graphene nanocomposite with disordered graphene, J. Nucl. Mater. 510 (2018) 1–9.
[9] L. Ji, F. Chen, H. Huang, X. Sun, Y. Yan, X. Tang, Preparation of nickel–graphene composites by jet electrodeposition and the influence of graphene oxide concentration on the morphologies and properties, Surf. Coating. Technol. 351 (2018) 212–219.
[10] Y. Ouyang, G. Yu, L. Hu, X. Wang, W. Xu, Y. Zhan, X. Zhang, Influence of Ni or Pd coatings on oxidation of permeated hydrogen, Surf. Eng. 29 (2013) 312–317.
[11] F. Liu, H. Zhou, X.-C. Li, Y. Xu, Z. An, H. Mao, W. Xing, Q. Hou, G.-N. Luo, Deuterium gas-driven permeation and subsequent retention in rolled tungsten foils, J. Nucl. Mater. 455 (2014) 248–252.

[12] J.P. Foster, D.L. Porter, D. Harrod, T. Mager, M. Burke, 316 stainless steel cavity swelling in a PWR, J. Nucl. Mater. 224 (1995) 207–215.

[13] M. Kupka, K. Stępień, K. Nowak, Studies on hydrogen diffusivity in iron aluminides using the Devanathan–Stachurski method, J. Phys. Chem. Solid. 75 (2014) 344–350.

[14] S. Xiukui, X. Jian, L. Yiyi, Hydrogen permeation behaviour in austenitic stainless steels, Mater. Sci. Eng., A 114 (1989) 179–187.

[15] P. Zhou, W. Li, H. Zhao, X. Jin, Role of microstructure on electrochemical hydrogen permeation properties in advanced high strength steels, Int. J. Hydrogen Energy 43 (2018) 10905–10914.

[16] C. Man, Z. Duan, Z. Cui, C. Dong, D. Kong, T. Liu, S. Chen, X. Wang, The effect of sub-grain structure on intergranular corrosion of 316L stainless steel fabricated via selective laser melting, Mater. Lett. 243 (2019) 157–160.

[17] Y.J. Oh, J.H. Hong, Nitrogen effect on precipitation and sensitization in cold-worked Type 316L (N) stainless steels, J. Nucl. Mater. 278 (2000) 242–250.

[18] S.-P. Hannula, H. Hänninen, S. Tähtinen, Influence of nitrogen alloying on hydrogen embrittlement in AISI 304-type stainless steels, Metall. Trans. A 15 (1984) 2205–2211.

[19] Y. Mine, K. Tachibana, Z. Horita, Grain-boundary diffusion and precipitate trapping of hydrogen in ultrafine-grained austenitic stainless steels processed by high-pressure torsion, Mater. Sci. Eng., A 528 (2011) 8100–8105.

[20] G. Alefeld, J. Völkl, Hydrogen in Metals I-Basic Properties, vol. 28, Springer-Verlag (Topics in Applied Physics, Berlin and New York, 1978, p. 442 (For individual items see A79-16057 to A79-16061), 1978.

[21] D.H.C.W. Jost, K. Hauffe, Diffusion 1, Fortschritte Der Physikalischen Chemie, 1972, pp. 155–196.

[22] Y.-P. Xu, F. Liu, S.-X. Zhao, X.-C. Li, J. Wang, Z.-Q. An, T. Lu, H.-D. Liu, F. Ding, H.-S. Zhou, Deuterium permeation behavior of HTUPS4 steel with thermal oxidation layer, Fusion Eng. Des. 113 (2016) 201–204.

[23] Q. Jia, D. Gu, Selective laser melting additive manufactured Inconel 718 superalloy parts: high-temperature oxidation property and its mechanisms, Optic Laser. Technol. 62 (2014) 161–171.

[24] Y. Zhou, S. Wen, B. Song, X. Zhou, Q. Teng, Q. Wei, Y. Shi, A novel titanium alloy manufactured by selective laser melting: microstructure, high temperature oxidation resistance, Mater. Des. 89 (2016) 1199–1204.

[25] A. Oudriss, J. Creus, J. Bouhattate, E. Conforto, C. Berziou, C. Savall, X. Feaugas, Grain size and grain-boundary effects on diffusion and trapping of hydrogen in pure nickel, Acta Mater. 60 (2012) 6814–6828.

[26] S. Frappart, X. Feaugas, J. Creus, F. Thebault, L. Delattre, H. Marchebois, Study of the hydrogen diffusion and segregation into Fe–C–Mo martensitic HSLA steel using electrochemical permeation test, J. Phys. Chem. Solid. 71 (2010) 1467–1479.

[27] E.G. Seebauer, A. Kong, L. Schmidt, Surface diffusion of hydrogen and CO on Rh (111): laser-induced thermal desorption studies, J. Chem. Phys. 88 (1988) 6597–6604.

[28] J. Leblond, D. Dubois, A general mathematical description of hydrogen diffusion in steels—I. Derivation of diffusion equations from Boltzmann-type transport equations, Acta Metall. 31 (1983) 1459–1469.

[29] Y.-F. Li, L.-M. Zhao, H.-L. Pan, Hydrogen permeation behaviour and associated phase transformations in annealed AISI304 stainless steels, Mater. Struct. 46 (2013) 621–627.

[30] L. Zhang, H.-j. Shen, J.-y. Sun, Y.-n. Sun, Y.-C. Fang, W.-h. Cao, Y.-y. Xing, M.-x. Lu, Effect of calcareous deposits on hydrogen permeation in X80 steel under cathodic protection, Mater. Chem. Phys. 207 (2018) 123–129.

[31] X.W. Zhou, R. Dingreville, R.A. Karnesky, Molecular dynamics studies of irradiation effects on hydrogen isotope diffusion through nickel crystals and grain boundaries, Phys. Chem. Chem. Phys. 20 (2018) 520–534.

[32] N. Yazdipour, A. Haq, K. Muzaka, E. Pereloma, 2D modelling of the effect of grain size on hydrogen diffusion in X70 steel, Comput. Mater. Sci. 56 (2012) 49–57.

[33] A.-M. Brass, J. Chêne, Hydrogen uptake in 316L stainless steel: consequences on the tensile properties, Corrosion Sci. 48 (2006) 3222–3242.

[34] H. Ohkubo, S. Sugiyama, K. Fukuzato, M. Takenaka, N. Tsukuda, E. Kuramoto, Positron-lifetime study of electrically hydrogen charged Ni, austenitic stainless steel and Fe, J. Nucl. Mater. 283 (2000) 858–862.

[35] Y. Chen, Y. Wu, Z. Wang, S. Wang, Positron annihilation study on interaction between hydrogen and defects in AISI 304 stainless steel, Radiat. Phys. Chem. 76 (2007) 308–312.

[36] C. He, T. Yoshiie, Q. Xu, K. Sato, S. Peneva, T. Troev, Detection of hydrogen in neutron-irradiated nickel using positron lifetime spectroscopy, Philos. Mag. A 89 (2009) 1183–1195.

[37] D. Segers, S. Van Petegem, J.F. Löffler, H. Van Swygenhoven, W. Wagner, C. Dauwe, Positron annihilation study of nanocrystalline iron, Nanostruct. Mater. 12 (1999) 1059–1062.

[38] M. Puska, R. Nieminen, Defect spectroscopy with positrons: a general calculational method, J. Phys. F Met. Phys. 13 (1983) 333.

[39] H. Sugimoto, Y. Fukai, Hydrogen-induced superabundant vacancy formation in bcc Fe: Monte Carlo simulation, Acta Mater. 67 (2014) 418–429.

[40] T. Nishiue, Y. Kaneno, H. Inoue, T. Takasugi, Thermal hydrogen desorption behavior of cathodically charged Ni3 (Si, Ti) alloys, J. Alloys Compd. 364 (2004) 214–220.

[41] X. Wang, L.N. Carter, B. Pang, M.M. Attallah, M.H. Loretto, Microstructure and yield strength of SLM-fabricated CM247LC Ni-Superalloy, Acta Mater. 128 (2017) 87–95.

[42] H. Yao, Z. Tan, D. He, Z. Zhou, Z. Zhou, Y. Xue, L. Cui, L. Chen, G. Wang, Y. Yang, High strength and ductility AlCrFeNiV high entropy alloy with hierarchically heterogeneous microstructure prepared by selective laser melting, J. Alloys Compd. 813 (2020), 152196.

[43] O. Ignatenko, I. Pokhodnya, Hydrogen induced localized plasticity in iron with BCC lattice. Proc. Of the 18th European Conf. on Fracture (ECF-18):«Fracture of Materials and Structure from Micro to Macroscale», Dresden, 2010, p. 2010.

[44] S.G. Chowdhury, S. Das, P. De, Cold rolling behaviour and textural evolution in AISI 316L austenitic stainless steel, Acta Mater. 53 (2005) 3951–3959.

[45] C. Senöz, S. Evers, M. Stratmann, M. Rohwerder, Scanning Kelvin probe as a highly sensitive tool for detecting hydrogen permeation with high local resolution, Electrochem. Commun. 13 (2011) 1542–1545.

[46] L. Reich, K. Svegh, J. Lendvai, A. Vertes, Positron lifetime study of an Al-1.7 at.% Mg-1.1 at.% Cu alloy, Phil. Mag. Lett. 81 (2001) 145–151.

[47] S. Li, Y. Li, Y.-C. Lo, T. Neeraj, R. Srinivasan, X. Ding, J. Sun, L. Qi, P. Gumbsch, J. Li, The interaction of dislocations and hydrogen-vacancy complexes and its importance for deformation-induced proto nano-voids formation in α-Fe, Int. J. Plast. 74 (2015) 175–191.

[48] V. Schlosser, Influence of processing temperature on minority carrier diffusion length of lower purity silicon, Z. Phys. B Condens. Matter 67 (1987) 453–458.

[49] S. Wang, K. Takahashi, N. Hashimoto, S. Isobe, S. Ohnuki, Strain field of interstitial hydrogen atom in body-centered cubic iron and its effect on hydrogen–dislocation interaction, Scripta Mater. 68 (2013) 249–252.